

# SCI: A spectrum concentrated implicit neural compression for biomedical data

Runzhao Yang<sup>1</sup>, Tingxiong Xiao<sup>1</sup>, Yuxiao Cheng<sup>1</sup>, Qianni Cao<sup>2</sup>, Jinyuan Qu<sup>1</sup>, Jinli Suo<sup>1,3</sup>,  
Qionghai Dai<sup>1</sup>

<sup>1</sup>Department of Automation, Tsinghua University, Beijing 100084, China

<sup>2</sup>Department of Electrical Engineering, Tsinghua University, Beijing 100084, China

<sup>3</sup>jlsuo@tsinghua.edu.cn

## Abstract

Massive collection and explosive growth of biomedical data, demands effective compression for efficient storage, transmission and sharing. Readily available visual data compression techniques have been studied extensively but tailored for natural images/videos, and thus show limited performance on biomedical data which are of different features and larger diversity. Emerging implicit neural representation (INR) is gaining momentum and demonstrates high promise for fitting diverse visual data in target-data-specific manner, but a general compression scheme covering diverse biomedical data is so far absent. To address this issue, we firstly derive a mathematical explanation for INR’s spectrum concentration property and an analytical insight on the design of INR based compressor. Further, we propose an adaptive compression approach SCI, which adaptively partitions the complex biomedical data into blocks matching INR’s concentrated spectrum envelop, and design a funnel shaped neural network capable of representing each block with a small number of parameters. Based on this design, we conduct compression via optimization under given budget and allocate the available parameters with high representation accuracy. The experiments show SCI’s superior performance to state-of-the-art methods including commercial compressors, data-driven ones, and INR based counterparts on diverse biomedical data. All the reproducible codes are going to be released on github.

## Introduction

Over decades, digital visual information is most commonly represented as discrete intensity values over a regularly spaced grid. Such straightforward representation is highly redundant, so a bunch of compression tools have been developed, such as MPEG/JPEG (Wallace 1992), H.264 (Wiegand et al. 2003), HEVC (Sullivan et al. 2012), etc. In spite of their successful applications and widespread acceptance, most of these compression techniques are tailored for natural images/videos and of limited performance in many domain specific visual data, such as biomedical images/volumes, which are of different characteristics and larger diversity than natural scenes.

With the resurgence of deep neural networks, a type of new representation of visual data is emerging—Implicit Neural Representation (INR), which uses a neural network

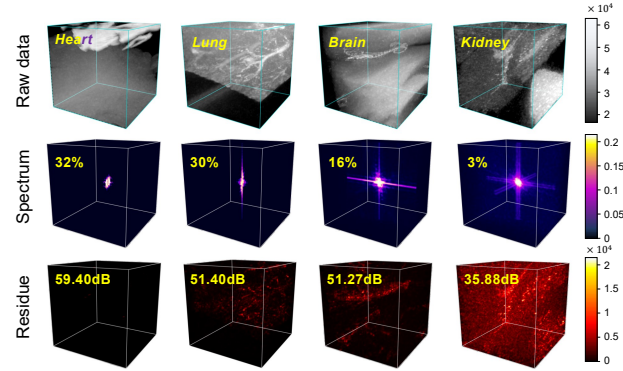


Figure 1: INR’s diverse compression capability on different biomedical data (from HiP-CT dataset), under  $64\times$  compression ratio. Top: several representative CT data of different organs, which are of increasing complexities from left to right. Middle: the corresponding spectrum (Fourier coefficients), with the percentage of non-zero entries labeled. Bottom: the residue after compression, which increases dramatically with the spreading range of the spectrum, with the reconstruction fidelity labeled in terms of PSNR.

to parameterize the data with an implicit continuous function. Specifically, for a visual data, the intensity at a voxel coordinate can be described by a neural function. Different from conventional discrete grid-based representations, INR is defined over a continuous space, and thus better matches the continuity property of the target visual information and is intrinsically independent of the discretization levels. Besides, according to the universal approximation theorem of neural networks, an INR implemented with Multi-Layer Perceptron (MLP) can fit arbitrarily complex functions given sufficient parameters (Gallant and White 1988; Hornik, Stinchcombe, and White 1989; Hornik 1991; Cybenko 1989; Leshno et al. 1993; Pinkus 1999), which promises high fidelity representation (Hornik, Stinchcombe, and White 1989). Under the INR representation, if we can model the underlying correlations among the neural functions of a target visual data at a set of positions, a compact INR representation can be achieved (Lu et al. 2021; Chen et al. 2021). Such INR based compression is obtaining better performance than conventional techniques on natural images/videos, and holds big promise for biomedical data (or

other special domains) via pursuing optimal data specific INR under parameter budget.

In spite of the high performance on natural visual data, INR based compression does not perform equally well on complex biomedical data like CT, which is of diverse spectrum distribution. As shown in Fig. 1, the compression capability significantly decreases as the spectrum spreads, which leaves following key issues open for exploration:

- Why and how does a broad spectrum degrade INR’s compression capability?
- How to keep INR’s high compression capability on complex data with a broad spectrum?

To address the above issues, we start from analyzing the representation fidelity of INR from the spectrum perspective. The analysis reveals that INR is “spectrum concentrated” and thus of low accuracy for data with spectrum beyond INR’s spectrum envelop, which explicitly answers the first question well. Following this, we propose spectrum concentrated implicit neural compression (SCI) to boost the compression capability of INR in three ways. Firstly, we develop an adaptive partitioning strategy to divide the target data with wide spreading spectrum into spectrum concentrated blocks with similar spectrum coverage. Secondly, we design a funnel shaped INR structure for efficient data compression, in which the number of neurons in each layer is elaborately designed for covering the spectrum of the target data block. Thirdly we establish an allocation strategy for the available number of INR parameters among the blocks.

Experimentally, we evaluated SCI’s performance and validated its wide applicability on biological and medical data. For biological data we used the brain-wide neurons and vessels of mouse captured by our self-developed imaging system, which have sparsely dispersed structures and their brightness distributions vary greatly in the observed data, especially that certain fine structures have faint brightness. For medical data we used HiP-CT (Walsh et al. 2021), a public dataset containing data volumes of human organs from the tissue to cellular scales, which are of large diversity in both appearance (e.g., structure, contrast, brightness, and noise levels). All these biomedical data are of broad spectrum range. The results show that SCI can significantly improve the compression capability of the INR based compression (NeRF (Mildenhall et al. 2020), SIREN (Sitzmann et al. 2020), and NeRV (Chen et al. 2021)), and SCI even outperforms commercial compression techniques (JPEG (Wallace 1992), H.264 (Wiegand et al. 2003), and HEVC (Sullivan et al. 2012)), and data-driven deep learning approaches (DVC (Lu et al. 2019)), SGA+BB (Yang, Bamler, and Mandt 2020), and SSF (Agustsson et al. 2020)), especially on the complex data with broad spectrum.

To summarize, the technical contributions are as follows:

- A mathematical explanation to INR’s spectrum concentration property and theoretical analysis on how broad spectrum degrades INR based compression quality.
- An adaptive partitioning strategy, which divides data with spreading spectrum into blocks fit in the INR’s spectrum envelop.

- An elaborately designed INR architecture capable of representing the blocks with small number of parameters.
- A parameter allocation strategy adapting to the spectral coverage of data blocks to achieve best compression.
- SCI outperforms existing INR based compressions, data-driven deep learning approaches and even widely used commercial compression techniques on biomedical data.

## Related work

**Data compression.** Data compression is fundamental for data sharing and storage. The community has witnessed the great progress in this field, from the handcrafted transform coding based compression methods such as JPEG (Wallace 1992) and JPEG2000 (Skodras, Christopoulos, and Ebrahimi 2001), to the predictive coding compression methods, like H.264 (Wiegand et al. 2003) and HEVC (Sullivan et al. 2012). These techniques have been widely and successfully used in compression for natural scenes. Built on conventional coding methodology, researchers attempt to use deep learning-based methods (Lu et al. 2019; Minnen, Ballé, and Toderici 2018; Ballé et al. 2018; Yang, Bamler, and Mandt 2020), which take the form of an autoencoder or variational autoencoders, to learn the best transformation, quantization, entropy models, and prediction methods from data. Recently, researchers have proposed an end-to-end video compression method (Agustsson et al. 2020), using scale-space flow and scale-space warping as a generalization of flow and bilinear warping in the motion compensation step. These compression methods are either tailored for natural scenes other than biomedical data or training data dependent. Differently, our approach is designed for compact and high fidelity data fitting for diverse biomedical data.

**Implicit neural representation.** INR is an emerging revolutionary representation of visual information, including shape (Genova et al. 2019a,b), image (Mordvintsev et al. 2018; Radford, Metz, and Chintala 2015; Thies, Zollhöfer, and Nießner 2019), video (Chen et al. 2021; Xian et al. 2021), and natural scenes (Chabra et al. 2020; Martel et al. 2021; Mildenhall et al. 2020; Sitzmann, Zollhöfer, and Wetzstein 2019), etc. The representation capability of INR can be improved from proper design of network structure (Chen et al. 2021; Fathony et al. 2021; Lu et al. 2021), selection of activation function (Klocek et al. 2019; Mehta et al. 2021; Sitzmann et al. 2020), embedding (Benbarka et al. 2021; Mildenhall et al. 2020; Tancik et al. 2020; Zhong et al. 2019), and learning strategies such as manifold learning (Du et al. 2021; Mehta et al. 2021; Sitzmann et al. 2020; Sitzmann, Zollhöfer, and Wetzstein 2019), meta learning (Bergman, Kellnhofer, and Wetzstein 2021; Du et al. 2021; Tancik et al. 2021) and ensemble learning (Aftab and Morsali 2021; Kadarvish et al. 2021; Niemeyer and Geiger 2021). Similar to the conventional grid based discrete representations, one has to trade off between the number of neural network parameters and its representation capability. Therefore, visual data compression under the INR representation is inherently to pursue the optimal representation capability under given limited number of parameter. The proposed SCI in this paper bridges the gap between the INR and data

compression, and can leverage the latest advances in the INR research to raise the compression ratio significantly.

**Implicit neural compression.** Recently INR has also been used for data compression and achieved promising results (Chen et al. 2021; Lu et al. 2021). They fit the original discrete grid-based data with continuous implicit functions in a transform-coding-like manner, which takes advantage of the powerful representation capabilities of neural networks while avoiding the generalization problem of data-driven. These primary studies demonstrate the practicability of data compression under the INR description, but the potential has far from been fully explored. The work in this paper proposes a coding framework capable of fitting diverse visual data adaptively, and is a big step towards extensive exploitation of INR’s advantageous in visual data compression.

### Spectrum concentration property of INR

A deep understanding of mechanisms behind the INR’s fidelity degeneration on data with broad spectrum, to the best of our knowledge, is still absent. To fill this gap, we offer a novel perspective which theoretically analyzes how broad spectrum degrades INR’s accuracy, based on a three-layer INR architecture, which can be extended to more layers.

The first layer in INR conducts frequency mapping for the input vector  $\mathbf{v}$ , and the output  $\mathbf{z}^{(0)}$  can be described as

$$\mathbf{z}^{(0)} = \sin(\mathbf{W}^{(0)}\mathbf{v}) = \sin(\mathbf{\Omega}\mathbf{v}), \quad (1)$$

in which  $\mathbf{W}^{(0)}$  is the weighting matrix, and we replace  $\mathbf{W}^{(0)}\mathbf{v}$  with  $\mathbf{\Omega}\mathbf{v}$  to represent the input frequencies. The second layer takes the linear combination of above sinusoids at varying mapping frequencies as input, and the output of the  $h$ th node can be written as

$$\mathbf{z}_h^{(1)} = \sin(\mathbf{W}_h^{(1)} \sin(\mathbf{\Omega}\mathbf{v})) \quad (2)$$

with  $\mathbf{W}^{(1)}$  denoting the coefficients of higher order terms of the input frequencies, followed by a sinusoidal activation function. After using Euler formula and conducting Fourier series expansion we arrive at Eqs. (3) and (4) respectively

$$\mathbf{z}_h^{(1)} = \text{Im} \left\{ \prod_{k=0}^{K-1} \exp \left( j \mathbf{W}_{h,k}^{(1)} \sin(\mathbf{\Omega}_k \mathbf{v}) \right) \right\} \quad (3)$$

$$= \text{Im} \left\{ \sum_{t_0=-\infty}^{\infty} \dots \sum_{t_{K-1}=-\infty}^{\infty} \prod_{k=0}^{K-1} J_{t_k}(\mathbf{W}_{h,k}^{(1)}) \exp(j t_k \mathbf{\Omega}_k \mathbf{v}) \right\}, \quad (4)$$

in which we introduce Bessel function to exhibit the coefficients of input frequencies and their high order harmonics, and  $t_k \mathbf{\Omega}_k \mathbf{v}$  represents a linear combination of integer harmonics of the input frequencies, indicating expression capability of the INR architecture for a wide range of frequencies. By further derivation (detailed in the supplementary note 1), one can get

$$\mathbf{z}_h^{(1)} = \sum_{t_1, \dots, t_K = -\infty}^{\infty} \left( \prod_{k=0}^{K-1} J_{t_k}(\mathbf{W}_{h,k}^{(1)}) \right) \sin \left( \sum_{k=0}^{K-1} t_k \mathbf{\Omega}_k \mathbf{v} \right). \quad (5)$$

Considering the sharply decaying behavior of Bessel functions  $J_{t_k}(\mathbf{W}_{h,k}^{(1)})$ , the high order harmonics in  $\mathbf{z}_h^{(1)}$  tend to have tinier coefficients than the input frequencies. Further, the third (last) layer is again a linear combination of the  $\mathbf{z}_h^{(1)}$

$$f(\mathbf{v}) = \mathbf{w}^{(2)\top} \mathbf{z}^{(1)} = \mathbf{w}^{(2)\top} \sin(\mathbf{W}^{(1)} \sin(\mathbf{\Omega}\mathbf{v})). \quad (6)$$

On the whole, the above three-layer and even more layers INR architecture will act as an inductive bias, which focuses most energy of the output signal in a narrow band around the input frequencies  $\mathbf{\Omega}$ . We refer to this phenomenon as the spectrum concentration property of INR.

Considering such spectrum concentration property, INR is more suitable for representing data with narrow spectrum consisting of a very small number of input frequencies. In other words, complex data with very spreading spectrum would suffer from severe compression artifacts because it falls out of INR’s spectrum envelop.

It’s worth noting that we also tested wavelet based transforms to characterize the spectrum concentration but achieved inferior performance. Besides, since derived in the Fourier domain, after partitioning we do not need wavelet-like transforms with spatially localization properties.

### SCI: Spectrum concentrated implicit neural compression

Inspired by the above analysis, we propose SCI to boost the compression capability of INR from three perspectives, with the pipeline illustrated in Fig. 2. Firstly, we develop an adaptive partitioning strategy to divide the target data with far spreading spectrum distribution into spectrum concentrated blocks falling within INR’s spectrum envelop. Secondly, we elaborately design a funnel shaped INR architecture for efficient representation of the data block. Thirdly we establish a parameter allocation strategy based on the spectral characteristics of each block.

#### Adaptive partitioning

To flexibly match the spectrum characteristics of diverse biomedical data with different complexities, we design an adaptive partitioning strategy to divide the target data into spectrum concentrated blocks that can be described by only a small set of parameters. There are two key problems need to be addressed here: (1) How many blocks are required? (2) How to determine an optimal boundary between different blocks? Furthermore, we expected the partitioning approach to be of more advantageous features: firstly, to achieve a higher computational efficiency, the proposed scheme should be able to tackle the above two entangled problems simultaneously rather than an iterative search; secondly, the scheme can be applied for different data adaptively; besides, results can further shed light on the successive parameter allocation within each block.

Towards this goal, we implement our partitioning strategy by solving an optimization problem, which maximizes the within-block spectrum concentration. Specifically, without loss of generality, we introduced a tree data structure to provide a unified explicit representation for all possible

partitioning patterns of a given data. In an  $L$  level tree data structure, the root node  $\mathbf{x} \in \mathbb{R}^{S_1 \times \dots \times S_N \times c}$  represents the input data, with  $S_1 \times \dots \times S_N$  denoting the spatial coordinates of  $N$ -dimensional data and  $c$  denoting channels (e.g., color, frame, etc.). At finer levels,  $\mathbf{x}^{(l)} = \{\mathbf{x}_i^{(l)} \in \mathbb{R}^{S_1 \times \dots \times S_N \times c}, i = 1, 2, \dots, 2^{N(l-1)}\}$  represents a set of blocks with  $\mathbf{x}_i^{(l)}$  being the  $i$ th node at the  $l$ th level, and the dimension of the block is written as

$$S_n^l = S_n / 2^{N(l-1)}, n = 1, 2, \dots, N. \quad (7)$$

Base on the tree-structure, a partitioning scheme can be expressed as a tree, with binary node values  $a_i^{(l)} = 1$  indicating the  $i$ th node at level  $l$  is a leaf node with sufficiently concentrated spectrum or  $a_i^{(l)} = 0$  representing a non-leaf node that needs further partitioning for spectrum concentration. Then, we define an objective as Eq. (8) to explicitly model the within-block spectrum concentration for pursuing a good partitioning scheme

$$\min_A \sum_{a_i^{(l)} \in A} a_i^{(l)} * \frac{-D(\mathbf{x}_i^{(l)})}{2^{nl}}, \quad (8)$$

where  $D(\mathbf{x}_i^{(l)})$ , calculated by the ratio of the top  $M$  largest values in the spectrum of  $\mathbf{x}_i^{(l)}$  to the total spectrum, represents the degree of spectrum concentration of this block.  $S(\mathbf{x}_i^{(l)})$  denotes the spectrum of  $\mathbf{x}_i^{(l)}$

$$D(\mathbf{x}_i^{(l)}) = \frac{\sum_{m=1}^M \max(S(\mathbf{x}_i^{(l)}), m)}{\sum S(\mathbf{x}_i^{(l)})}, \quad (9)$$

and  $A$  denotes partitioning strategies

$$A := \bigcup_{l=1}^L \{a_i^{(l)}, i = 1, \dots, 2^{n(l-1)}\}. \quad (10)$$

To avoid exhaustive searching, we define the feasible set of our partitioning strategy for fast optimization

$$\sum_{a \in A} a \leq a_{max}, \quad (11)$$

$$\sum_{a \in P(a_j^{(L)})} a = 1, j = 1, \dots, 2^{n(L-1)}, \quad (12)$$

where  $P(\cdot)$  represents a path to the root node. Eq. (11) defines the upper bound of number of blocks, limited by a theoretical minimum number of parameters in MLP to maintain representation capability (Trenn 2008), and Eq. (12) is introduced following the tree data structure.

In this way, partitioning strategy is formulated into an ILP (Integer Linear Programming) problem which can be solved efficiently by state-of-the-art solvers. This partitioning is a universal one being able to adaptively determine the optimal number and boundary of blocks, based on the features of the target visual data and under the given compression ratio.

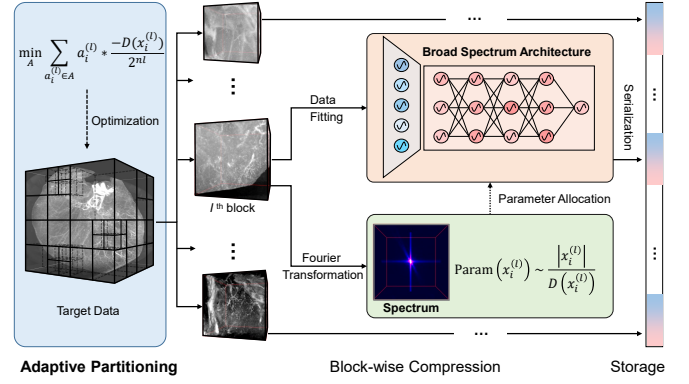


Figure 2: The flow chart of the proposed SCI. Firstly, the target data is adaptively partitioned into blocks (left) via solving an optimization problem, which favours a solution with all the blocks having similar spectrum coverage approximately matching the concentrated spectrum envelope of the adopted INR. Then SCI compresses each block separately with a funnel shaped neural network architecture (middle top). The parameters are allocated according to the spectral characteristics (middle bottom) and optimized to fit the target data block (data fitting). Afterwards, the network parameters (mainly weights and bias) of each INR are serialized into the final compressed data (right).

### Funnel shaped neural network architecture

After partitioning, we build a highly efficient INR architecture for block-wise data compression, in which the number of neurons for each layer is elaborately designed for covering the spectrum of the target data block and achieving high representation accuracy. For the first layer conducting frequency mapping, we allocate a wide set of neurons to increase the cardinality of  $\Omega$ . For the successive layers, we arrange fewer neurons at each layer to increase the depth of network. As mentioned above,  $\mathbf{W}^{(l)}$  controls the bandwidth of the frequency modulation including translation, multiplication and harmonic expansion. Given the limited parameters it's more efficient to increase the numbers of expansion, i.e. the depth rather than the width of network, i.e.  $|\mathbf{W}^{(l)}|$ , since the former would expand the spectral support exponentially. We denote the ratio between the number of neurons in the first layer and that in the subsequent layers by  $fr$

$$fr = |\mathbf{W}_{:,0}^{(0)}| / |\mathbf{W}_{:,0}^{(1)}|, \quad (13)$$

which is large than 1 here to take account of both the spectrum coverage and representation efficiency.

### Parameter allocation

Adopting the optimal partitioning strategy, the within-block spectrum concentration can be subsequently calculated. In this section, we go one step further and develop a parameter allocation strategy based on the spectral characteristics of each block. Our strategy leverages the within-block spectrum concentration to initialize the number of parameters allocated to each block.

Intuitively, a block with wider spectrum range (i.e., lower spectrum concentration) is more complex and deserves more parameters to maintain high reconstruction fidelity. Without loss of generality, we use an intuitive solution by setting the number of parameters allocated to each block to be proportional to its spectrum coverage. Taking  $\mathbf{x}_i^{(l)}$  as an example, the parameter number linearly increases with  $\frac{|\mathbf{x}_i^{(l)}|}{D(\mathbf{x}_i^{(l)})}$ , where  $|\mathbf{x}_i^{(l)}|$  denotes the size of  $\mathbf{x}_i^{(l)}$ .

## Experiments

### Implementation details

We evaluated our approach on both massive biological and medical data. For the former we used the mouse brain-wide microscopic data at sub-micrometer resolution (*Neurons* and *Vessels*), which have diverse brightness and structures among different regions. For the latter we used HiP-CT dataset (Walsh et al. 2021), providing cellular level imaging of different organisms at multiple anatomical levels. We used all the four human organs (*Lung*, *Heart*, *Kidney* and *Brain*) contained in the dataset.

For convenient and fair comparison, we cropped the data into the same size and used the raw data without pre-processing but simply normalizing the coordinates to  $[-1, 1]^3$  in INR based methods.

For our approach, the network includes 7 layers,  $fr = 2.2$ , the hyper parameter of sinusoidal frequency  $w_0 = 20$ , and is optimized by Adamax (Kingma and Ba 2014) with learning rate of 0.001. During partitioning, we set  $M = 1$  and  $a_{max} = 50$  by default empirically.

The weights and bias of network are serialized and stored in binary, and some necessary information for decompression are stored in a small YAML file, including the network structure, original data bit depth, image size, inverse normalization basic information, etc. Due to the fact that all of the items are discrete data, countable and limited in the set of their possible values, we can easily create a table listing all potential values and store the index, allowing the file to be very small.

Because both compression and decompression are conducted in block-wise manner, we have to record the block information. The position and size of each block is recorded in the name of its compressed file, e.g., for a  $16 \times 128 \times 128$  block starting from  $(0, 256, 0)$  is named as “*d\_0\_15 – h\_256\_383 – w\_0\_127*”. In addition, the length of file name is much smaller than the limit of modern file systems. Moreover, there might exist block artifacts in the decoded version, especially at high compression ratio, and we use the adaptive deblocking filter (List et al. 2003) to address this issue.

### Benchmark methods and evaluation metrics

The proposed method is comprehensively compared with state-of-the-art methods, which are classified into three groups: (i) widely used commercial compression techniques, including JPEG (Wallace 1992), H.264 (Wiegand et al. 2003), and HEVC (Sullivan et al. 2012); (ii) recently proposed data-driven deep learning based ones, in-

cluding DVC (Lu et al. 2019), SGA+BB (Yang, Bamler, and Mandt 2020), and SSF (Agustsson et al. 2020); (iii) INR based ones, including SIREN (Sitzmann et al. 2020), NeRF (Mildenhall et al. 2020), and NeRV (Chen et al. 2021). All methods were evaluated at the similar compression ratios (only INR based methods can precisely regulate the compression ratio). We denoted the real compression ratio by BPV (bits per voxel), and use the same performance metrics to evaluate their compression performance. We use Accuracy with threshold for binarization as evaluation metrics for biological data with sparse structures, while PSNR and SSIM for medical data including rich details.

We used off-the-shelf implementations to evaluate the widely used commercial compression methods. JPEG was tested with its OpenCV implementation. H.264 and HEVC were tested on FFmpeg with specified bit rate settings and the applicable highest bit depth, i.e., 10-bit for H.264 and 12-bit for HEVC. In terms of data-driven methods, i.e. DVC, SGA+BB, and SSF, we fine-tuned the provided pre-trained models on 300 volumes ( $16 \times 256 \times 256$  voxels) randomly selected from the dataset. For SGA+BB, we used the setting with the highest performance mentioned in the original paper. For DVC, we used the Pytorch implementation, and the “I Frames” were compressed using JPEG method (with quality parameter set to 50). For SSF, we adopted the CompressAI’s implementation and adjusted the compression ratio by setting its quality parameters. For INR based compression, SIREN and NeRF were both equipped with a 7-layer network structure and  $fr = 1$ . For SIREN, its hyper parameter  $w_0 \in [10, 40]$ . For NeRF, the hyper parameter “frequency” was set to 10. For NeRV, we control the compression ratio by adjusting the number and width of the fully connected layers. Note that for 2D image compression methods, i.e. JPEG and SGA+BB, we firstly flattened our volumetric data before compression.

The average performance of each method on different compression ratios is plotted as a rate-distortion curve in Fig. 3. It is worth noting that our method outperforms state-of-the-art methods at almost all BPVs, showing its great capability at varying compression ratios on both biological and medical data.

For more detailed analysis, we summarize the scores on each dataset in Table 1. Since only the INR based method can control the BPV precisely, the others fluctuate around the specified BPV, we calculate the average performance of all the algorithms within the intersection of their BPVs range on each dataset. Generally, our method and HEVC rank top two on all organs from CT. Since our method is a lossy compression and tends to suppress noise, on noisier data such as *Lung* and *Kidney*, our method is slightly inferior to HEVC on SSIM, while on cleaner data such as *Heart* and *Brain*, the PSNR of our method surpasses HEVC by 1.69dB and 0.51dB respectively. For *Neurons* and *Vessels*, the INR based methods have significant advantages and ours works best.

It should be noted that unlike the compression of natural images, the PSNR is generally high for medical data. Therefore, even though the PSNR is higher than 40dB, it does not mean that there is no distortion in the visual effect, which is

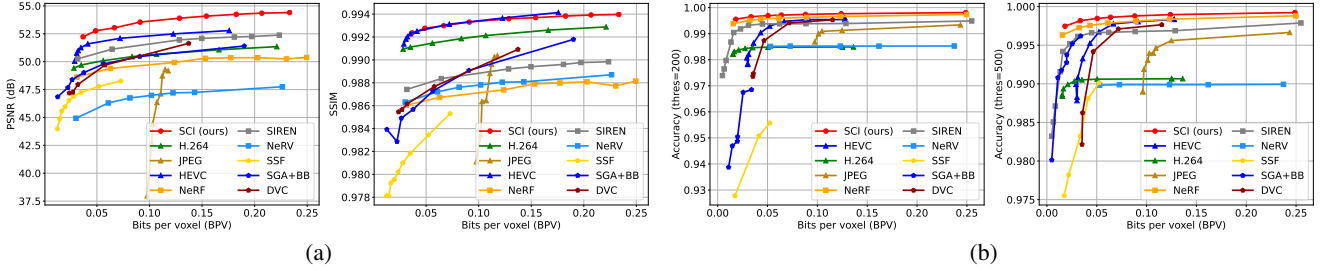


Figure 3: Comparison of different compression methods on medical (a) and biological data (b) at different BPVs.

Table 1: The average metrics on each dataset as BPV ranges from 0.01 to 0.25, with the **best** and the **second best** marked by color. The metrics include PSNR(dB), SSIM, and Accuracy( $\tau$ ) with  $\tau$  acts as a threshold for binarization.

Method	<i>Lung</i>		<i>Heart</i>		<i>Kidney</i>		<i>Brain</i>		<i>Neurons</i>		<i>Vessels</i>	
	PSNR	SSIM	PSNR	SSIM	PSNR	SSIM	PSNR	SSIM	Acc. (200)	Acc. (500)	Acc. (200)	Acc. (500)
SCI (ours)	<b>45.63</b>	<b>0.9734</b>	<b>63.23</b>	<b>0.9995</b>	<b>50.15</b>	<b>0.9896</b>	<b>50.82</b>	<b>0.9927</b>	<b>0.9986</b>	<b>0.9995</b>	<b>0.9944</b>	<b>0.9970</b>
JPEG	42.32	0.9599	48.20	0.9970	44.76	0.9850	43.90	0.9757	0.9949	0.9969	0.9846	0.9866
H.264	45.30	0.9733	57.66	0.9990	49.59	0.9894	50.08	0.9925	0.9950	0.9975	0.9710	0.9797
HEVC	<b>46.15</b>	<b>0.9763</b>	<b>61.54</b>	<b>0.9992</b>	<b>50.09</b>	<b>0.9902</b>	<b>50.31</b>	<b>0.9932</b>	0.9947	0.9976	0.9848	0.9891
SIREN	45.48	0.9727	55.49	0.9989	48.99	0.9891	49.22	0.9905	<b>0.9983</b>	<b>0.9993</b>	0.9866	0.9918
NeRF	44.56	0.9687	57.77	0.9991	49.77	0.9890	49.77	0.9919	0.9980	0.9992	<b>0.9913</b>	<b>0.9949</b>
NeRV	43.36	0.9681	53.67	0.9982	46.71	0.9887	46.83	0.9908	0.9948	0.9970	0.9756	0.9828
DVC	44.42	0.9698	54.36	0.9987	48.75	0.9887	47.19	0.9887	0.9935	0.9970	0.9828	0.9901
SGA+BB	44.95	0.9700	54.38	0.9977	48.51	0.9875	48.68	0.9887	0.9920	0.9957	0.9620	0.9803
SSF	43.12	0.9643	52.98	0.9980	46.86	0.9865	46.92	0.9901	0.9850	0.9951	0.9504	0.9525

closely related to the type of target data.

Some visual comparisons of decompressed organ slices are reported in Fig. 4 (see Supplementary Figures 1,2, and 3 for more results). We did the same post-processing on the decompressed data for better visual comparison. At similar BPV around 256 $\times$ (since SGA+BB and HEVC cannot precisely regulate compression ratio), we consistently outperform existing INR based (NeRV and NeRF), data-driven deep learning (SGA+BB) and commercial compression methods (HEVC). NeRF produces blurry artifacts on most of informative regions, since the broad spectrum of the target data goes beyond the spectrum envelop of the network. NeRV retains the general structures but suffers from the block artifacts caused by the aliasing in convolution. In the depressed results of SGA+BB, one can notice checkerboard artifacts in the regions with rich details. HEVC is able to capture details in “I Frames” well but there exist severe block artifacts in “P Frames”. This can distort the edges in the volumes, such as the tubules in Fig. 4’s rows 1-3 and white and grey matters in rows 4-6, which would be unusable for medical research as well as other downstream tasks. In addition, HEVC struggles with the ghosting artifacts from neighbor slices in “P Frames”, causing position offset in some regions, which would result in discontinuous 3D structure, after decompression, leading to wrong medical diagnosis or incorrect results in downstream tasks. On the contrary, the proposed approach is of the highest fidelity after decompression.

## Ablation studies

We validated our adaptive partitioning, network architecture design, and parameter allocation strategy via an extensive ablation study, with the results shown in Table 2 (see Supplementary Table.1 for detailed results on each dataset). The first row shows the performance of our complete model as a reference. The complete model adopted adaptive partitioning, funnel shaped network architecture (i.e., more neurons in the first layer than in successive layers), and spectrum-width proportional parameter allocation. In rows 2-8, we removed one of these three components at a time from the complete model to quantitatively evaluate their contribution to the final performance.

Table 2: Results of ablation studies on medical and biological data.

Method	<i>Medical data</i>		<i>Biological data</i>	
	PSNR	SSIM	Acc. (200)	Acc. (500)
SCI (ours)	<b>49.29</b>	<b>0.9558</b>	<b>0.9752</b>	<b>0.9865</b>
EP	48.67	0.9546	0.9706	0.9842
NP	47.76	0.9532	0.9670	0.9835
$fr = 1.0$	49.24	0.9556	0.9537	0.9738
$fr < 1.0$	48.87	0.9540	0.9354	0.9600
By Size	49.01	0.9560	0.9708	0.9849
By $D$	48.82	0.9558	0.9745	0.9861
Equal	48.35	0.9554	0.9707	0.9855

In rows 2-3, we removed adaptive partitioning and adopted either naive equidistant partitioning (EP) or no partitioning (NP). The comparison between reconstruction fi-

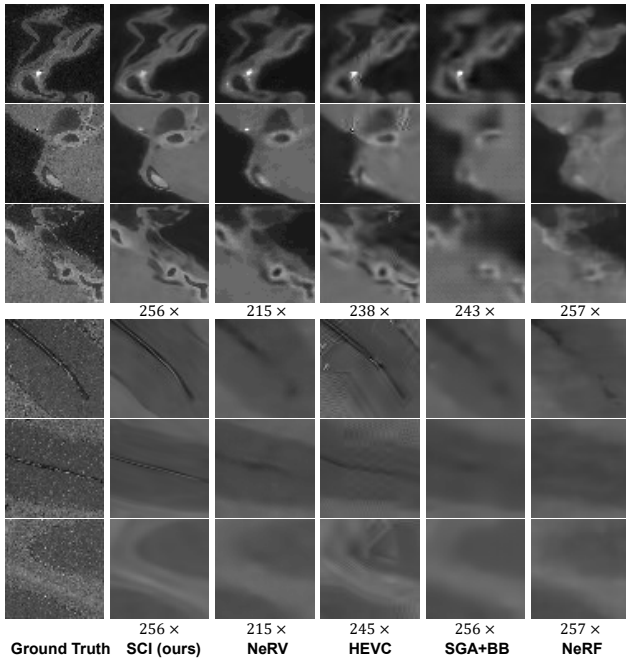


Figure 4: Visual comparisons with state-of-the-arts on medical data—2D slices from 3D volumes. Rows 1-3 show the regions-of-interest (ROIs) of tubules on kidney. Rows 4-6 show the ROIs of white and grey matters on brain. The compression ratios are labeled at bottom.

delity of models with adaptive partitioning and without partitioning under various BPVs on medical data are shown in Fig. 5 (see Supplementary Figure. 4 for detailed results on all the datasets). Applying adaptive partitioning according to the spectrum concentration of data tend to achieve higher reconstruction fidelity than that without partitioning, which indicates the necessity of adaptive partitioning. It is worth noting that the performance of no-partitioning strategy decreases as BPV increases, since the neural network is too large to optimize. In all the cases, adaptive partitioning is consistently better than equidistant partitioning.

Rows 4–5 show how the performance decreases as  $fr$  reduces. One can see that for almost all the test data, the reconstruction fidelity consistently gets higher when using a funnel shaped architecture with larger opening, i.e., wider spectrum coverage. Experimentally, the optimal ratio  $fr$  varies with the target data and compression ratio.

In our approach, the number of parameters of each block is proportional to  $\frac{|\mathbf{x}_i^{(l)}|}{D(\mathbf{x}_i^{(l)})}$ . In rows 6-8, we compared our parameter allocation scheme with three different adhoc counterparts: the number of allocated parameters in rows 6-7 is proportional to  $|\mathbf{x}_i^{(l)}|$  and  $\frac{1}{D(\mathbf{x}_i^{(l)})}$  respectively; the 8th row shows the result by equally allocating parameters among data blocks. Compared with the last three rows we can conclude that allocating parameters based on the concentration of data spectrum indeed can improve the compression performance.

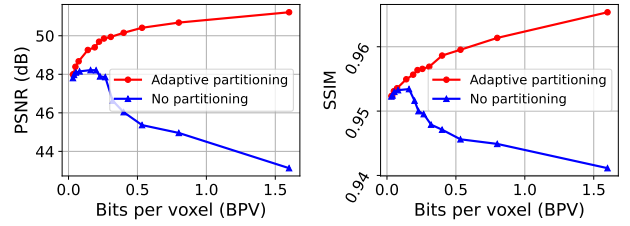


Figure 5: Comparison between SCI’s reconstruction fidelity with adaptive partitioning and without partitioning on medical data, in terms of PSNR and SSIM.

Summarizing all the ablation studies, three strategies all contribute to the final high performance, and the improvement is consistent over all the test data. Comparatively, the adaptive partitioning brings the largest quantitative benefit.

In addition, the reasonableness of using  $D(\mathbf{x}_i^{(l)})$  to express the data spectrum concentration is demonstrated by the experimental results in the Supplementary Figure. 5.

## Conclusions

In this paper we report a general INR based compression approach for massive diverse biomedical data. The proposed approach is built on a mathematical analysis of the INR’s spectrum concentration property, and theoretical exploration on the mechanisms behind the performance variation over diverse data with different spectrum coverages. Based on the analytical insight, we proposed an adaptive partitioning strategy for addressing spectrum-spreading data, an elaborately designed INR architecture for efficient data compression, and a parameter allocation strategy for further performance boosting. Experiments indicate that our method outperforms state-of-the-art methods including conventional (JPEG, H.264, HEVC), data-driven (DVC, SGA+BB, SSF), and existing INR based ones (SIREN, NeRF, NeRV) on a large diversity of biological and medical data. Our method inherits the benefit of INR, such as the ability to precisely regulate the compression ratio and the freedom to tailor fidelity of different local regions. This paper is a pioneering study, which will pave the way for compression on the emerging neural representation.

**Limitations.** As an emerging technique, our approach is limited in several aspects. Firstly, current implementation requires relatively longer time than commercial compression methods, since it takes time to search for the proper network parameters fitting the target data. Secondly, we only remove within-block redundancy, taking inter-block redundancy into consideration (similar to incorporating non-local similarity) can further improve the compression. We expect to devote more efforts on acceleration and performance boosting of this promising new compression approach.

**Future work.** We plan to combine meta-learning to find the manifold of a specific biomedical data in INR space and equip with the CUDA implementation to boost SCI’s speed and accuracy. It is also a worth studying topic to combine network compression for shortening the coding length and non-local ensemble for removing inter-block redundancy.

## References

- Aftab, A.; and Morsali, A. 2021. Multi-Head ReLU Implicit Neural Representation Networks. *arXiv preprint arXiv:2110.03448*.
- Agustsson, E.; Minnen, D.; Johnston, N.; Balle, J.; Hwang, S. J.; and Toderici, G. 2020. Scale-space flow for end-to-end optimized video compression. In *Proceedings of the IEEE/CVF Conference on Computer Vision and Pattern Recognition*, 8503–8512.
- Ballé, J.; Minnen, D.; Singh, S.; Hwang, S. J.; and Johnston, N. 2018. Variational Image Compression with a Scale Hyperprior. In *International Conference on Learning Representations*.
- Benbarka, N.; Höfer, T.; Zell, A.; et al. 2021. Seeing Implicit Neural Representations as Fourier Series. *arXiv preprint arXiv:2109.00249*.
- Bergman, A. W.; Kellnhofer, P.; and Wetzstein, G. 2021. Fast Training of Neural Lumigraph Representations using Meta Learning. In *Advances in Neural Information Processing Systems*.
- Chabra, R.; Lenssen, J. E.; Ilg, E.; Schmidt, T.; Straub, J.; Lovegrove, S.; and Newcombe, R. 2020. Deep Local Shapes: Learning Local SDF Priors for Detailed 3D Reconstruction. In *European Conference on Computer Vision*, 608–625.
- Chen, H.; He, B.; Wang, H.; Ren, Y.; Lim, S. N.; and Shrivastava, A. 2021. NeRV: Neural Representations for Videos. *Advances in Neural Information Processing Systems*.
- Cybenko, G. 1989. Approximation by Superpositions of a Sigmoidal Function. *Mathematics of Control, Signals and Systems*.
- Du, Y.; Collins, K.; Tenenbaum, J.; and Sitzmann, V. 2021. Learning Signal-agnostic Manifolds of Neural Fields. *Advances in Neural Information Processing Systems*.
- Fathony, R.; Sahu, A. K.; Willmott, D.; and Kolter, J. Z. 2021. Multiplicative Filter Networks. In *International Conference on Learning Representations*.
- Gallant, A. R.; and White, H. 1988. There Exists a Neural Network that does not Make Avoidable Mistakes. In *IEEE International Conference on Neural Networks*, 657–664 vol.1.
- Genova, K.; Cole, F.; Sud, A.; Sarna, A.; and Funkhouser, T. A. 2019a. Deep Structured Implicit Functions. *Computing Research Repository*.
- Genova, K.; Cole, F.; Vlastic, D.; Sarna, A.; Freeman, W. T.; and Funkhouser, T. 2019b. Learning Shape Templates with Structured Implicit Functions. In *Proceedings of the IEEE/CVF International Conference on Computer Vision*.
- Hornik, K. 1991. Approximation Capabilities of Multilayer Feedforward Networks. *Neural Networks*, 4(2): 251–257.
- Hornik, K.; Stinchcombe, M.; and White, H. 1989. Multilayer Feedforward Networks Are Universal Approximators. *Neural Networks*, 2(5): 359–366.
- Kadarvish, M. S.; Mojtahedi, H.; Zarch, H. E.; Kazerouni, A.; Morsali, A.; Abtahi, A.; and Marvasti, F. 2021. Ensemble Neural Representation Networks. *arXiv preprint arXiv:2110.04124*.
- Kingma, D. P.; and Ba, J. 2014. Adam: A Method for Stochastic Optimization. *arXiv preprint arXiv:1412.6980*.
- Klocek, S.; Maziarka, Ł.; Wołczyk, M.; Tabor, J.; Nowak, J.; and Śmieja, M. 2019. Hypernetwork Functional Image Representation. In *International Conference on Artificial Neural Networks*, 496–510.
- Leshno, M.; Lin, V. Y.; Pinkus, A.; and Schocken, S. 1993. Multilayer Feedforward Networks with a Nonpolynomial Activation Function can Approximate any Function. *Neural Networks*, 6(6): 861–867.
- List, P.; Joch, A.; Lainema, J.; Bjontegaard, G.; and Karczewicz, M. 2003. Adaptive Deblocking Filter. *IEEE Transactions on Circuits and Systems for Video Technology*, 13(7): 614–619.
- Lu, G.; Ouyang, W.; Xu, D.; Zhang, X.; Cai, C.; and Gao, Z. 2019. DVC: An End-to-end Deep Video Compression Framework. In *Proceedings of the IEEE/CVF Conference on Computer Vision and Pattern Recognition*, 11006–11015.
- Lu, Y.; Jiang, K.; Levine, J. A.; and Berger, M. 2021. Compressive Neural Representations of Volumetric Scalar Fields. *Computer Graphics Forum*, 40(3): 135–146.
- Martel, J. N.; Lindell, D. B.; Lin, C. Z.; Chan, E. R.; Monteiro, M.; and Wetzstein, G. 2021. ACORN: Adaptive Coordinate Networks for Neural Scene Representation. *arXiv preprint arXiv:2105.02788*.
- Mehta, I.; Gharbi, M.; Barnes, C.; Shechtman, E.; Ramamoorthi, R.; and Chandraker, M. 2021. Modulated Periodic Activations for Generalizable Local Functional Representations. *arXiv preprint arXiv:2104.03960*.
- Mildenhall, B.; Srinivasan, P. P.; Tancik, M.; Barron, J. T.; Ramamoorthi, R.; and Ng, R. 2020. NeRF: Representing Scenes as Neural Radiance Fields for View Synthesis. In *European Conference on Computer Vision*, 405–421.
- Minnen, D.; Ballé, J.; and Toderici, G. D. 2018. Joint Autoregressive and Hierarchical Priors for Learned Image Compression. In *Advances in Neural Information Processing Systems*, volume 31.
- Mordvintsev, A.; Pezzotti, N.; Schubert, L.; and Olah, C. 2018. Differentiable Image Parameterizations. *Distill*, 3(7): e12.
- Niemeyer, M.; and Geiger, A. 2021. Giraffe: Representing Scenes as Compositional Generative Neural Feature Fields. In *Proceedings of the IEEE/CVF Conference on Computer Vision and Pattern Recognition*, 11453–11464.
- Pinkus, A. 1999. Approximation Theory of the MLP Model in Neural Networks. *Acta Numerica*, 8: 143–195.
- Radford, A.; Metz, L.; and Chintala, S. 2015. Unsupervised Representation Learning with Deep Convolutional Generative Adversarial Networks. *arXiv preprint arXiv:1511.06434*.

Sitzmann, V.; Martel, J. N. P.; Bergman, A. W.; Lindell, D. B.; and Wetzstein, G. 2020. Implicit Neural Representations with Periodic Activation Functions. In *Advances in Neural Information Processing Systems*.

Sitzmann, V.; Zollhöfer, M.; and Wetzstein, G. 2019. Scene Representation Networks: Continuous 3D-Structure-Aware Neural Scene Representations. *arXiv preprint arXiv:1906.01618*.

Skodras, A.; Christopoulos, C.; and Ebrahimi, T. 2001. The JPEG 2000 Still Image Compression Standard. *IEEE Signal Processing Magazine*, 18(5): 36–58.

Sullivan, G. J.; Ohm, J.-R.; Han, W.-J.; and Wiegand, T. 2012. Overview of the High Efficiency Video Coding (HEVC) Standard. *IEEE Transactions on Circuits and Systems for Video Technology*, 22(12): 1649–1668.

Tancik, M.; Mildenhall, B.; Wang, T.; Schmidt, D.; Srinivasan, P. P.; Barron, J. T.; and Ng, R. 2021. Learned Initializations for Optimizing Coordinate-based Neural Representations. In *Proceedings of the IEEE/CVF Conference on Computer Vision and Pattern Recognition*, 2846–2855.

Tancik, M.; Srinivasan, P. P.; Mildenhall, B.; Fridovich-Keil, S.; Raghavan, N.; Singhal, U.; Ramamoorthi, R.; Barron, J. T.; and Ng, R. 2020. Fourier Features Let Networks Learn High Frequency Functions in Low Dimensional Domains. In *Advances in Neural Information Processing Systems*.

Thies, J.; Zollhöfer, M.; and Nießner, M. 2019. Deferred Neural Rendering: Image Synthesis using Neural Textures. *ACM Transactions on Graphics*, 38(4): 1–12.

Trenn, S. 2008. Multilayer Perceptrons: Approximation Order and Necessary Number of Hidden Units. *IEEE Transactions on Neural Networks*, 19(5): 836–844.

Wallace, G. K. 1992. The JPEG Still Picture Compression Standard. *IEEE Transactions on Consumer Electronics*, 38(1): xviii–xxxiv.

Walsh, C.; Tafforeau, P.; Wagner, W.; Jafree, D.; Bellier, A.; Werlein, C.; Kühnel, M.; Boller, E.; Walker-Samuel, S.; Robertus, J.; et al. 2021. Imaging Intact Human Organs with Local Resolution of Cellular Structures using Hierarchical Phase-Contrast Tomography. *Nature Methods*, 18(12): 1532–1541.

Wiegand, T.; Sullivan, G. J.; Bjontegaard, G.; and Luthra, A. 2003. Overview of the H.264/AVC Video Coding Standard. *IEEE Transactions on Circuits and Systems for Video Technology*, 13(7): 560–576.

Xian, W.; Huang, J.-B.; Kopf, J.; and Kim, C. 2021. Space-time Neural Irradiance Fields for Free-viewpoint Video. In *Proceedings of the IEEE/CVF Conference on Computer Vision and Pattern Recognition*, 9421–9431.

Yang, Y.; Bamler, R.; and Mandt, S. 2020. Improving Inference for Neural Image Compression. In *Advances in Neural Information Processing Systems*, volume 33, 573–584.

Zhong, E. D.; Bepler, T.; Davis, J. H.; and Berger, B. 2019. Reconstructing Continuous Distributions of 3D Protein Structure from Cryo-EM Images. *arXiv preprint arXiv:1909.05215*.

## Supplementary Notes

### 1. Derivation for Eq(2)-Eq(5)

$$z_h^{(1)} = \sin(\mathbf{W}_h^{(1)} \sin(\boldsymbol{\Omega} \mathbf{v})) \quad (1)$$

$$= \sin \left( \sum_{k=0}^{K-1} \mathbf{W}_{h,k}^{(1)} \sin(\boldsymbol{\Omega}_k \mathbf{v}) \right) \quad (2)$$

$$= \text{Im} \left\{ \exp \left( j \left( \sum_{k=0}^{K-1} \mathbf{W}_{h,k}^{(1)} \sin(\boldsymbol{\Omega}_k \mathbf{v}) \right) \right) \right\} \quad (3)$$

$$= \text{Im} \left\{ \prod_{k=0}^{K-1} \exp \left( j \mathbf{W}_{h,k}^{(1)} \sin(\boldsymbol{\Omega}_k \mathbf{v}) \right) \right\} \quad (4)$$

$$= \text{Im} \left\{ \prod_{k=0}^{K-1} \sum_{t_k=-\infty}^{\infty} J_{t_k} \mathbf{W}_{h,k}^{(1)} \exp(j t_k \boldsymbol{\Omega}_k \mathbf{v}) \right\} \quad (5)$$

$$= \text{Im} \left\{ \sum_{t_0=-\infty}^{\infty} \dots \sum_{t_{K-1}=-\infty}^{\infty} \prod_{k=0}^{K-1} J_{t_k} \mathbf{W}_{h,k}^{(1)} \exp(j t_k \boldsymbol{\Omega}_k \mathbf{v}) \right\} \quad (6)$$

$$= \sum_{t_1, \dots, t_K=-\infty}^{\infty} \text{Im} \left\{ \left( \prod_{k=0}^{K-1} J_{t_k} \mathbf{W}_{h,k}^{(1)} \right) \exp \left( j \sum_{k=0}^{K-1} t_k \boldsymbol{\Omega}_k \mathbf{r} \right) \right\} \quad (7)$$

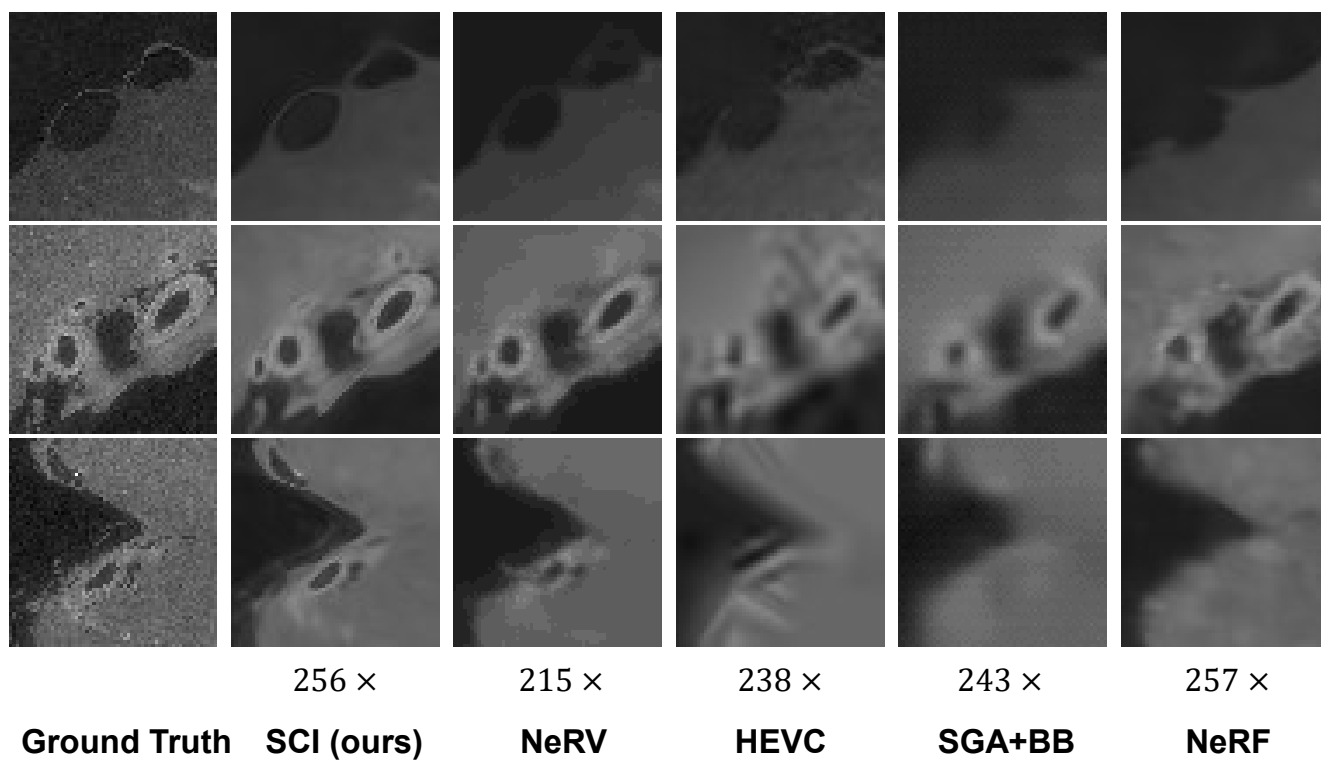
$$= \sum_{t_1, \dots, t_K=-\infty}^{\infty} \left( \prod_{k=0}^{K-1} J_{t_k} \mathbf{W}_{h,k}^{(1)} \right) \text{Im} \left\{ \exp \left( j \sum_{k=0}^{K-1} t_k \boldsymbol{\Omega}_k \mathbf{r} \right) \right\} \quad (8)$$

$$= \sum_{t_1, \dots, t_K=-\infty}^{\infty} \left( \prod_{k=0}^{K-1} J_{t_k} \mathbf{W}_{h,k}^{(1)} \right) \sin \left( \sum_{k=0}^{K-1} t_k \boldsymbol{\Omega}_k \mathbf{r} \right) \quad (9)$$

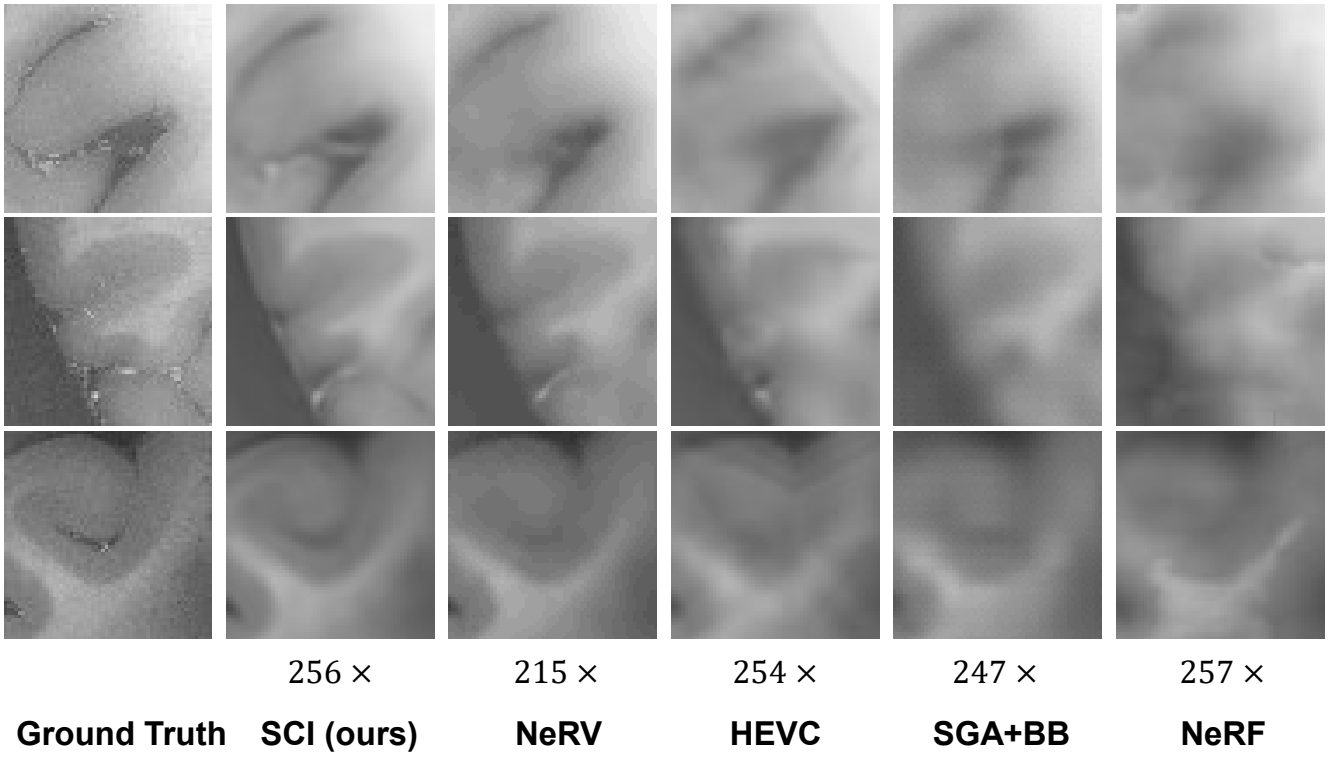
where  $J_m(\cdot)$  represents the Bessel function of the first kind of order  $m$  and (5) follows from the Fourier series expansion of  $\exp(jw \sin(x))$ :

$$\exp(jw \sin(x)) = \sum_{m=-\infty}^{\infty} J_m(w) \exp(jm x). \quad (10)$$

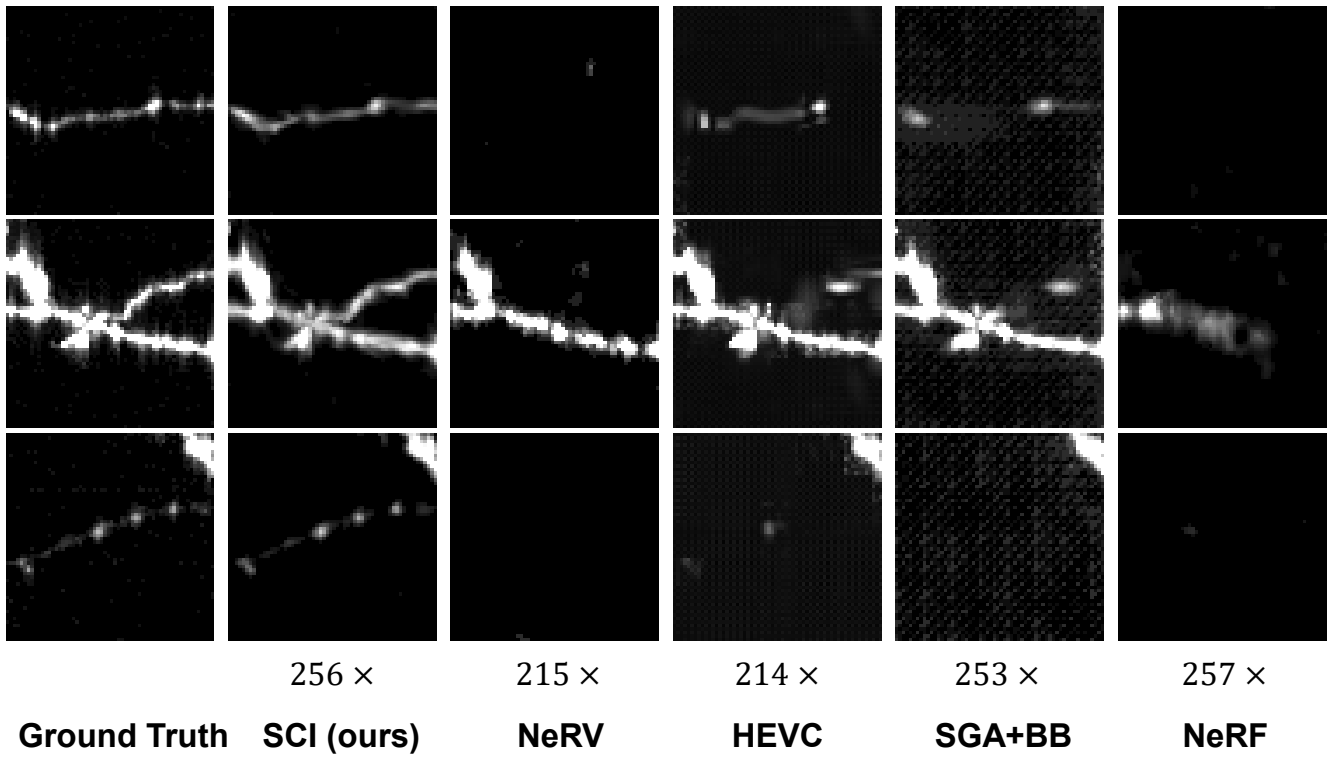
## Supplementary Figures



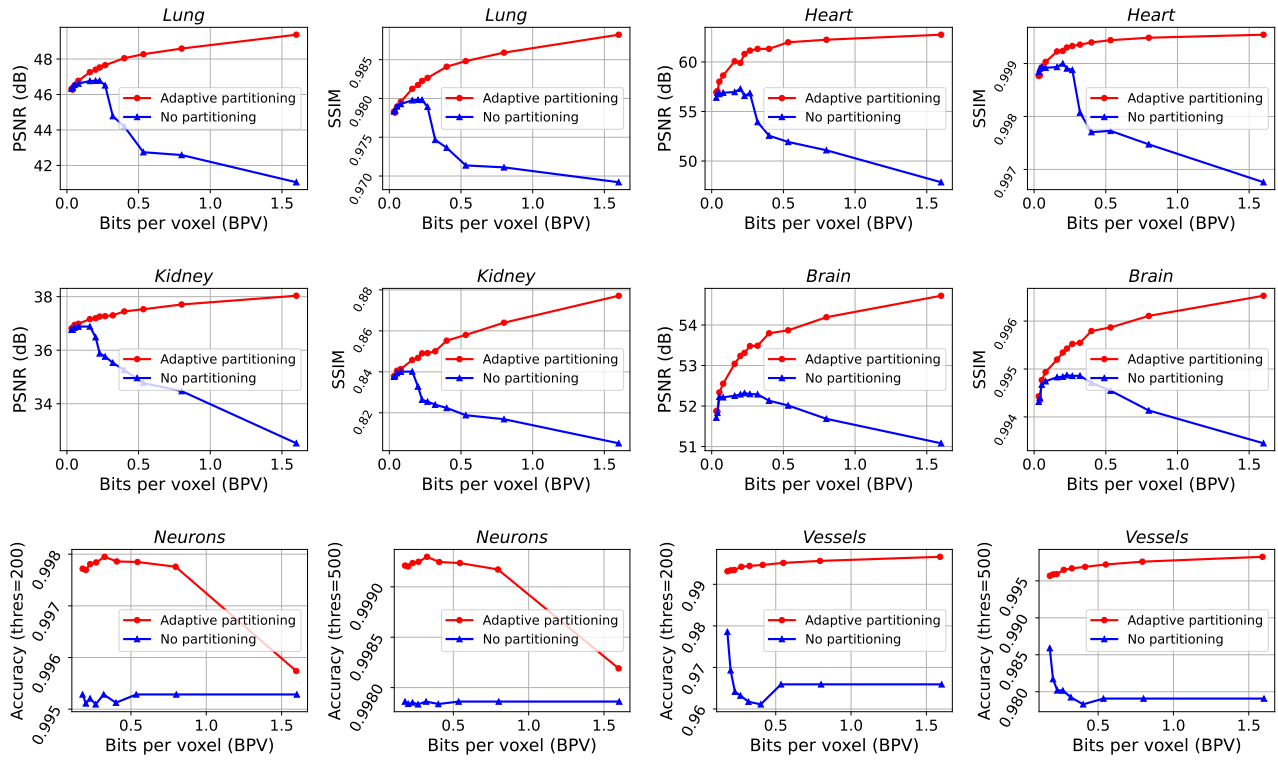
Supplementary Figure. 1. Visual comparisons with state-of-the-arts on *Kidney* dataset—2D slices from 3D volumes. The compression ratio of each are labeled at bottom.



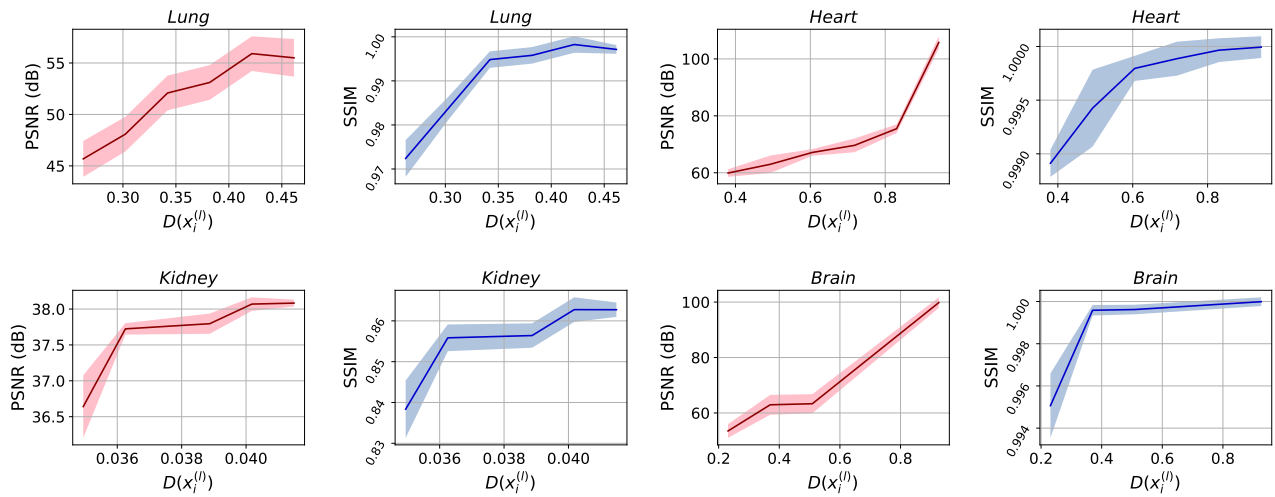
Supplementary Figure. 2. Visual comparisons with state-of-the-arts on *Brain* dataset—2D slices from 3D volumes. The compression ratio of each are labeled at bottom.



Supplementary Figure. 3. Visual comparisons with state-of-the-arts on *Neurons* dataset—2D maximum intensity projections from 3D volumes. The compression ratio of each are labeled at bottom.



Supplementary Figure. 4. Comparison between the reconstruction fidelity of our compressor with adaptive partitioning and without partitioning on each dataset.



Supplementary Figure. 5. Statistical graph of the relationship between reconstruction fidelity and the degree of spectrum concentration on each dataset (denoted by  $D(x_i^{(l)})$ ). One can find a significant positive correlation between them.

## Supplementary Tables

Supplementary Table. 1. The ablation study of our model on each dataset. We used compression ratio  $80\times$ , data size  $256 \times 256 \times 256$  voxels, iteration number 10,000 for medical data and compression ratio  $100\times$ , data size  $16 \times 512 \times 512$  voxels, iteration number 10,000 for biological data.

Method	<i>Lung</i>		<i>Heart</i>		<i>Kidney</i>		<i>Brain</i>		<i>Neurons</i>		<i>Vessels</i>	
	PSNR	SSIM	PSNR	SSIM	PSNR	SSIM	PSNR	SSIM	Acc.(200)	Acc.(500)	Acc.(200)	Acc.(500)
SCI (ours)	<b>47.46</b>	<b>0.9820</b>	<b>59.49</b>	<b>0.9993</b>	<b>37.18</b>	<b>0.8464</b>	<b>53.02</b>	<b>0.9953</b>	<b>0.9944</b>	<b>0.9970</b>	<b>0.9560</b>	<b>0.9760</b>
EP	46.81	0.9805	58.84	0.9992	36.96	0.8437	52.06	0.9950	0.9940	0.9967	0.9471	0.9716
NP	46.68	0.9795	55.95	0.9989	36.84	0.8394	51.58	0.9948	0.9880	0.9922	0.9460	0.9747
$fr = 1.0$	47.41	0.9819	59.44	0.9993	37.15	0.8459	52.97	0.9952	0.9922	0.9955	0.9151	0.9521
$fr < 1.0$	47.05	0.9807	59.03	0.9992	36.91	0.8414	52.47	0.9948	0.9847	0.9919	0.8860	0.9281
By Size	47.41	0.9818	58.52	0.9992	37.13	0.8474	52.97	0.9953	0.9939	0.9966	0.9476	0.9731
By $D$	47.27	0.9815	57.97	0.9992	37.10	0.8472	52.95	0.9954	0.9942	0.9968	0.9548	0.9753
Equal	47.04	0.9809	56.60	0.9990	37.01	0.8467	52.74	0.9951	0.9941	0.9967	0.9473	0.9742